Optical diagnostics of mercury jet for an intense proton target

H. Park,[1] T. Tsang,[2] H. G. Kirk,[2] F. Ladeinde,[1,a)] V. B. Graves,[3] P. T. Spampinato,[3] A. J. Carroll,[3] P. H. Titus,[4] and K. T. McDonald[5]

[1]*SUNY at Stony Brook, New York 11794, USA*
[2]*Brookhaven National Laboratory, Upton, New York 11973, USA*
[3]*Oak Ridge National Laboratory, Oak Ridge, Tennessee 37831, USA*
[4]*Massachusetts Institute of Technology, Cambridge, Massachusetts 02139, USA*
[5]*Princeton University, Princeton, New Jersey 08544, USA*

An optical diagnostic system is designed and constructed for imaging a free mercury jet interacting with a high intensity proton beam in a pulsed high-field solenoid magnet. The optical imaging system employs a backilluminated, laser shadow photography technique. Object illumination and image capture are transmitted through radiation-hard multimode optical fibers and flexible coherent imaging fibers. A retroreflected illumination design allows the entire passive imaging system to fit inside the bore of the solenoid magnet. A sequence of synchronized short laser light pulses are used to freeze the transient events, and the images are recorded by several high speed charge coupled devices. Quantitative and qualitative data analysis using image processing based on probability approach is described. The characteristics of free mercury jet as a high power target for beam-jet interaction at various levels of the magnetic induction field is reported in this paper. © *2008 American Institute of Physics.* [DOI: 10.1063/1.2912820]

I. INTRODUCTION

Neutrino factories and muon colliders require a large number of muons, which are obtained from the decay of pions. Efficient production of pions can be achieved by colliding an intense proton beam with a high-Z target. The choice of the target material is an important issue. Over the past years, several target materials have been proposed, including copper, graphite, and mercury, with recent emphasis on the latter materials.[1] An important consideration is the problem of removing the power deposited by the proton beam without interfering with the process of extracting the end product, which is the muon beam. When proton beam energy reaches ~100 kJ/pulse, the heat from the beam could melt or crack a stationary solid high-Z target. Hence, a recyclable moving liquid mercury (Hg) jet is proposed as a preferred target candidate. Efficient capture of low-energy secondary pions requires that the target be positioned in a strong magnetic induction field, which will also stabilize the mercury flow. However, many other technical challenges remain. The beam energy varies depending on the beam kinetic energy, the number of protons, and beam bunches per pulse. The response of a liquid target in a high magnetic induction field will have beam energy effects, which needs to be experimentally investigated. In order to better understand the dynamics of mercury flow in a high magnetic induction field and its subsequent interaction with the proton beam, the mercury intense target (MERIT) experiment has been developed in our work as a proof-of-principle experiment to address target issues. To this end, experiments on the interaction of 14 and 24 GeV proton beams with the pulse structures of 4 to 16 bunches per pulse and the spot size of 1.6 mm rms up to 30×10^{12} protons per pulse has been carried out at CERN.

The Hg delivery system generates a jet of approximately 1 cm, constant diameter with velocities up to 20 m/s in a 15 T magnetic field.[2] The primary diagnostic of the beam-jet interaction is optical, employing the technique of a backilluminated laser shadow photography. Due to the intense radiation environment and limited space inside the bore of the magnet, passive radiation-hard optical components and fibers are used to illuminate and observe the motion of the mercury jet. In addition, incorporating a retroreflecting mirror in the imaging system simplifies and miniaturizes the laser backillumination scheme. A set of four viewports along the interaction region are connected by flexible coherent imaging fiber bundles to four high speed cameras to independently and simultaneously record the dispersal of mercury that results from beam-jet interaction. Images are frozen either by a sequence of short laser light pulses and/or by the short exposure time set on the cameras.

The mercury loop system, the pulsed solenoid magnet, and the optical diagnostic system are designed and constructed at ORNL, MIT Plasma Science and Fusion Center, and BNL, respectively. The performance of the optical diagnostic system is presented, along with the results of integrated system testing with pulsing of the mercury jet in the pulsed high-field magnet.

II. TARGET ISSUES

A liquid mercury target has advantages over a solid target because a flowing jet can readily remove the heat load and it is immune to radiation damage. However, a liquid mercury target poses two critical challenges. First, the penetration of a conducting liquid jet into the magnetic induction field can result in target deformation. Second, the fragmen-

---

tation of the liquid metal due to the intense and sudden heating by the proton beam can result in magnetohydrodynamic (MHD) instabilities. These instabilities can change the shape of the jet, resulting in a significantly less efficient target for pion production. Furthermore, moving mercury in a magnetic induction field causes induced eddy currents, which cause the mercury jet to experience axial retardation and radial compressive forces upon entry into the field. Axial currents are also induced if the jet axis does not align with the axis of the magnetic induction field. These axial currents will produce transverse elliptical distortions of the mercury jet. It is important to tilt the target and proton beam relating to the axis of solenoid magnet so that the pions that leave the side of the target are not reabsorbed after one turn on their helical trajectory.[3] To this end, an inclination angle of 33 milliradian for the jet axis with respect to the axis of solenoid magnet was used in the experiment. This tilt angle determines the subsequent pion/muon collection. For the mercury jet to present a new target of two interaction lengths on each macropulse, the mercury velocity is required to reach 20 m/s. The mercury target should be in the form of a free jet, rather than confined in a pipe, because the beam-induced cavitation of the liquid metal is detrimental to any solid wall in the immediate vicinity of the interaction region.

III. OPTICAL DIAGNOSTIC METHOD

Direct visualization techniques for hydrodynamic examination have often been employed to investigate the dynamics of MHD flows. In this method, one measures the time taken for the particles to traverse a given path. Because no quantitative results can be deduced from direct visualization methods and difficulties often arise when investigating thin boundary layers in liquids, attention has turned to the use of optical techniques for the investigations of fluid dynamics and MHD.[4]

Optical techniques are noninvasive and do not cause any perturbation of the subject being investigated. Furthermore, their sensitivity increases with photon intensity and the resolution of the subject can reach the diffraction-limited resolution. The optical response of fluid dynamics and MHD are practically instantaneous, enabling the optical technique to study details of turbulent flows and transition states. Coupled to a state-of-the-art high speed camera and the long interaction path length of a light beam with a field of view adjustable to arbitrary dimensions, the optical technique enables one to obtain the physical characteristics for the entire subject being investigated in a short period of time.

A. Shadow photography

One of the most common optical shadow photography techniques is Schlieren photography, in which a parallel light beam passes through an optically inhomogeneous subject in a homogeneous surrounding medium. A portion of the light beam will deviate by a certain angle at the edge of the inhomogeneous subject, causing additional path length leading to optical interference with the unperturbed part of the beam. The results from this work reveal the outline of the perturbation with good image characteristics. However, due to the
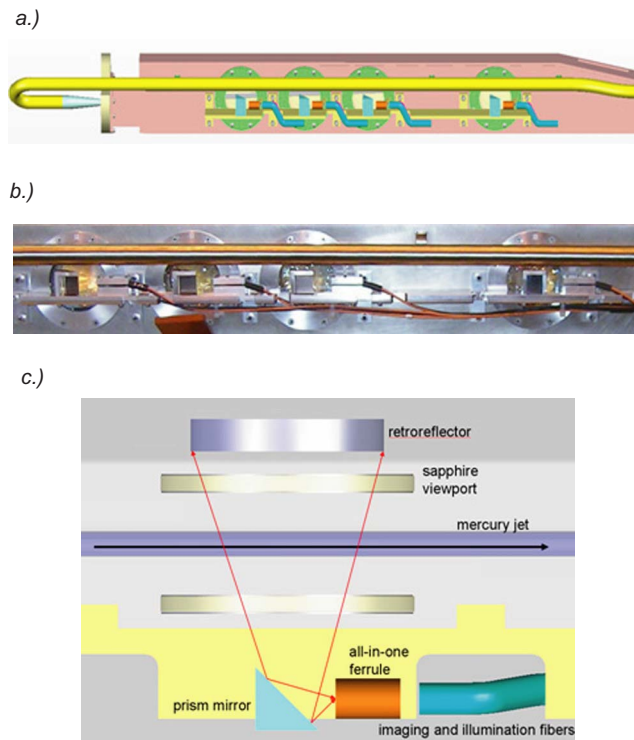

FIG. 1. (Color online) Design of optical layout and installation of four viewports of primary containment vessel. (a) Conceptual integration of optics to primary containment vessel. (b) Photograph of installation of optics to primary containment vessel. (c) Schematic layout of optical components.

limited space inside the bore of a cryogenically cooled magnet and the fact that a free mercury jet is completely opaque under conventional lighting, a simple optical diagnostic system based on backilluminated shadow photography is employed in the present study. This simple optical imaging system provides adequate image quality for quantitative jet dynamics, yet it is compact enough to fit inside the bore of the magnet together with other mercury delivery pipes and associated monitoring devices. A similar laser backilluminated imaging system but with much larger physical dimensions was used in earlier experiments with successful results.[1,5,6]

B. Optical diagnostics design

Laser backilluminated shadow photography technique is employed in the present work to capture the dynamics of the interaction of the proton beam with a moving free mercury jet. The design of the optical imaging system is based on a few essential criteria which are described below. The entire optical imaging head has to fit inside a small portion of a 1 m long, 150 mm diameter bore magnet. Figures 1(a)–1(c) show the conceptual backilluminated optics design, the installation of four viewports on the primary containment vessel, and the schematic layout of optical components, respectively.

Another design criterion for the optical imaging system pertains to the mercury toxicity and its vapor presents even prior to beam interactions. Although the mercury jet is confined to propagate inside a completely airtight stainless steel primary containment vessel with sealed optics, minute
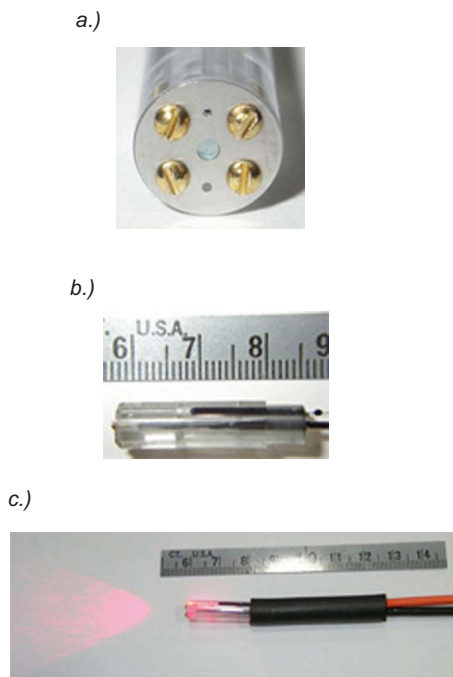
FIG. 2. (Color online) Photograph of optical head assembly and its illumination of laser. (a) Front view of optical head assembly. (b) Side view of optical head assembly. (c) Illumination of fiber-optics head assembly.

FIG. 3. (Color online) Polished fiber end, 50× and 800× magnifications, respectively.

amount of mercury vapor can potentially reside between the primary and secondary containment vessels after each hydraulic pulsing of the mercury jet. Since the optical heads are directly attached on the primary containment vessel, it could pose a health hazard to people in close proximity to the instrument. Therefore, the optical heads use only passive optical components and are designed to be service-free once mercury is loaded into the system and when the secondary containment vessel is completely enclosed.

Note that all optics placed inside the interaction beam tunnel are required to be radiation hard because of high radiation levels in the beam tunnel and the activation of the mercury after proton beam interactions. In our setup, all cameras, lasers, and all other associated electronics are placed in an adjacent beam tunnel locally controlled by several desktop computers. Remote control of the entire system is achieved through designated control desktops located in the control room via MS Window XP remote desktop connections from the Ethernet network (see Fig. 5).

A viewport is located at the beam interaction center and two additional viewports are located at ±152.4 mm up/down stream locations. Viewport 4 is positioned at +457.2 mm and is designed to capture the residual dynamics of the proton interaction. Because of the limited space inside the magnet bore, object illumination and image capture are transmitted through multimode optical fibers and coherent imaging fibers, respectively, all positioned on one side exterior to the primary containment vessel. Figure 2 shows the in-house fabricated and assembled optical head containing the integration of ball lens, imaging lens, illumination fiber, and imaging fiber.

The arrangement resembles a compact endoscope design but with a different illumination scheme. Illumination light
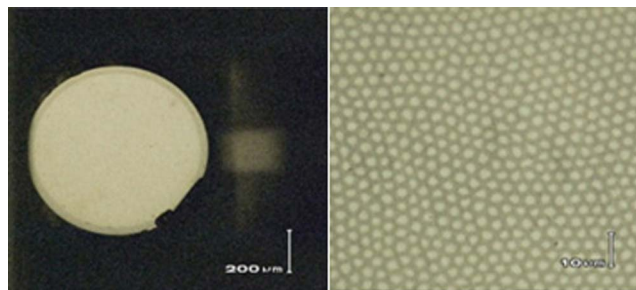
pulses are coupled into a 15 m long multimode fiber (Thor-Labs BFL22-200). It has a numerical aperture of 0.22, 25° cone angle, with a core diameter of 200 μm that matches that of the fiber-coupled lasers. To provide a ~55 mm illumination area at the center of the primary containment vessel over a limited short working distance of <100 mm, the illumination cone angle has to be opened up to a 43° full cone angle. This is achieved by placing a tiny ~0.5 mm diameter sapphire ball lens (Edmund Optics M46-117) at the tip of the illumination fiber and secured by a thin stainless steel plate. At the heart of the illumination arrangement is a 76 mm diameter Au-coated concave spherical retro-reflector that has a short radius of curvature of 124 mm (Rainbow Research Optics). When the much diverged illumination fiber is placed at the radius of curvature and shined onto the optical axis of the reflector, a retroreflected beam returns back to the illumination fiber providing the backillumination scheme. Again, because of the tight environment inside the primary, a Au-coated 90° prism mirror turns the optical path from longitudinal to transverse onto the center of the primary. Two antireflection coated sapphire windows (Swiss Jewel Company) are mounted on the primary with airtight seals tested up to 1.4 bar pressure. The diameter and the thickness of the window are 100 and 6 mm, respectively, sufficiently large enough for the observation of a 1 cm diameter jet and mechanically strong enough to withstand the momentum of a direct impact from mercury jet with a mean velocity of 20 m/s.[7]

Based on this optical arrangement, a mercury jet in front of the reflector naturally makes a shadow on the retroreflected beam. The shadow is collected by a tiny 1 mm diameter antireflection-coated cylindrical grin objective lens (GrinTech, GT-IFRL-100-inf-50-CC) which has an optical path length of 2.43 mm. The grin lens is butt coupled onto a coherent image fiber. This flexible coherent imaging fiber is the key optical element of the imaging system. It is a 10 m long Sumitomo IGN-08/30 fiber with 30 000 picture elements (pixels). Each individual fiber has a core diameter of ~4 μm with a total fiber diameter of merely 0.96 mm including coating. It has a bending radius of 40 mm, sufficiently small to allow curving and arching inside the primary containment vessel. All imaging fiber ends are hand polished in house to optical finished quality to allow high quality images with maximum light intensity transmission. Figure 3 shows the final finished end of an imaging fiber after polishing with 0.3 μm lapping film (ThorLabs, LFG03P).

TABLE I. Specifications of high speed cameras.

Attributes	SMD 64KIM	Fast Vision	Olympus Encore PCI 8000S
CCD chip size	13.4×13.4 mm^2	15.4×12.3 mm^2	$1/3$ in.
Pixels	960×960	1280×1024	480×420
Pixel size	14 μm	12 μm	13 μm
Single frame	240×240	1280×1000	480×420
Maximum frame rate	1 MHz[a]	0.5 kHz[b]	4 kHz[c]
Full well Capacity	$220\,000 e^-$	~ 1000 LSB/lux-sec	$\cdots$
ADC	12 bit	8 bit	8 bit

[a]16 frames.
[b]At full resolution.
[c]12.5 μs electronic shutter, with reduced frame size.

The surface quality and the flatness of the imaging fibers are inspected under a microscope. The imaging fibers are jacketed in house with reinforced furcation tubing (ThorLab FT030-BK). One end of the imaging fiber is finished with an SMA 905 fiber-optics connector to facilitate coupling to a charge coupled device (CCD) camera. The other ends of the illumination and imaging fibers are positioned next to each other with ~ 2 mm separation inserted inside a specially fabricated plastic ferrule. The integrated optical head is shown in Fig. 2, where a red laser diode is used to illuminate the optical head. The integrated all-in-one ferrule (ball lens, illumination fiber, objective lens, and imaging fiber bundle) is placed at the radius of curvature as well as on the optical axis of the reflector so that it allows both the illumination and the imaging collection to work on one side of the primary. The liquid mercury target is enclosed in a stainless steel primary containment vessel which is placed in the primary beam tunnel (TT2A). A total of four optical imaging heads for each viewport are mounted on the exterior of the primary, designated as channels 1–4. All fibers are routed through a ~ 150 mm diameter, 2 m long concrete passage to an adjacent beam tunnel (TT2), where radiation is much reduced. All electronics control for the optical diagnostic as well as all other electronics control for the solenoid magnet operation and hydraulic power unit used to generate the mercury jet are also placed in the adjacent tunnel. The exit end of each imaging fiber is coupled to an SMA fiber adaptor (ThorLabs SM1SMA) mounted on an *x-y* translator (ThorLab LM1XY). Four $40\times$ infinitely corrected microscope objective (Newport M-40x) relay the ~ 0.96 mm image outputs of each imaging fiber onto each corresponding CCD with appropriate lens tubes to fully expand the images onto a typical 10×10 mm CCD array. A nonrotating adjustable lens tube zoom housing (ThorLabs SM1ZM) provides fine and accurate adjustment of image focus on CCD.

C. High speed cameras and light sources

Table I gives the specifications of high speed cameras in terms of some selected attributes. Two FastVision cameras with CCD size of 15.4×12.3 mm^2 run with a full 1280×1000 pixel resolution at a 0.5 kHz frame rate. One Olympus Encore PCI 8000S camera with $1/3$ in. CCD size runs with a 480×420 pixel resolution at a 4 kHz recording rate. A high speed "Silica Mountain Devices (SMD)" 64KIM

camera with a CCD size of 13.4×13.4 mm^2 runs with a reduced single frame size of $(960 \times 960)/4$ pixel resolution at up to 1 MHz frame rate. For the three slower cameras, images collected by each individual imaging fiber overfill the CCD pixels by factors of ~ 6 and ~ 3, respectively, i.e., one fiber projected onto 6×6 and 3×3 CCD pixel area, respectively. However, for the SMD camera, each imaging fiber slightly underfills the CCD pixels by a factor of 0.83, i.e., one fiber projected onto nearly a single CCD pixel area. Due to the nature of spatial superposition, an array of imaging fibers imaged by an array of CCD pixels, some images might compose of a honeycomb pattern caused by this pixelation artifact. However, the artifact can be minimized by slightly defocusing the image on the CCD. However, the FastVision and Olympus CCDs are capable of recording at a frame rate higher than 500 Hz, the architecture for binning at reduced resolution requires a change of the zoom ratio on the image head doom. The SMD camera has a different but fixed binning architecture so that the full field of view is taken at a high speed frame rate with reduced resolution. Except for the SMD camera where images are frozen by the short 150 ns illumination laser pulses, all other images are arrested by the short adjustable electronic exposure time of $10-50$ μs set on the CCDs.

Synchronized short laser light pulses are used to illuminate the target and freeze the motion of the jet after the impact of the proton beam. Optical light pulses are sent through 15 m of multimode illumination fibers. The light sources used in the experiment are all class 4 lasers, emitting at wavelengths of $808-850$ nm. Three lasers are capable of emitting a peak optical power of 1 W (JDS Uniphase SDL-2300-L2) driven by three independent current drivers (ThorLabs LDC220C). These 1 W lasers can be operated from clockwise to a minimum programmable pulse width of 1 μs limited by the trigger logic pulse. The fourth laser emits at a peak optical power of 25 W (Bright Solution BDL20-808-F6) limited by the pulsed current driver (Avtech AXOZ-A1A-B). It provides a current pulse of 150 ns and is capable of running at the maximum 1 MHz repetition rate, i.e., a frame rate of 1 μs/frame.

The complete transmission of the imaging system is ~ 0.2 per viewport channel, including 0.85 for the 15 m long illumination fiber, 0.86 for the sapphire ball lens, 0.86 for each pass of the sapphire viewport, 0.91 for the retroreflec-

TABLE II. Effects of irradiation up to an equivalent radiation dose of 10^6 rad on the reflectance and transmittance of the components of the optical diagnostic system. Reflectance is inferred on the Au-coated mirror and transmittance is inferred on all other components.

Optical component	Before radiation	After radiation	% difference
Large Au-coated mirror	0.91	0.92	no change
Sapphire window (1 mm)	0.86	0.87	no change
Illumination fiber (5 m)	1	1.02	no change
Imaging fiber (30 cm)	0.67	0.71	no change
Grin lens	0.90	0.66	73%

tor, 0.67 for the 10 m long imaging fiber, and 0.86 for the grin lens and the relay lens. For the SMD camera, the imaging circle filled $\pi/4$ of the CCD array. A measured output energy of 3.5 μJ/pulse is obtained from the Bright Solution (BDL20-808-F6) laser illumination light source for viewport 2. Therefore, the calculated number of photons impinging on the SMD camera reaches 4.2×10^6 photons/pixel. After taking into account the 18% quantum efficiency of the CCD, 7.5×10^5 photoelectrons are generated at the full illumination intensity. Since the SMD camera has full well capacity of $2.2 \times 10^5 e^-$, there is a factor of ~ 3 on the optical power budget reserved for unanticipated optical power loss and for overcoming the possible attenuation due to ionization radiation. Similar calculations for viewport channels 1 and 3 give a factor of ~ 10 on the optical power budget. This larger factor is mostly due to the long, 10 μs, exposure time set on the FastVision cameras. Overall, the imaging system is designed to have sufficient optical power budget for the illumination of each viewport throughout the entire experiment.

D. Radiation hardness

Because of the high radiation level in the beam tunnel and the activation of the mercury after the proton beam interactions, all optics placed inside the interaction beam tunnel are required to be radiation hard. One complete set of optics was selected for radiation resistance test done at CERN. This complete set of optics included an Au-coated reflector, sapphire window, illumination fiber, imaging fiber, and Grin objective lens. The MERIT experiment has anticipated a total of 200 proton pulses at 14 and 24 GeV with a total of $\sim 3 \times 10^{15}$ protons. The calculated total radiation reaches $\sim 10^6$ rad equivalent radiation dose. Therefore, all optics except the grin objective lens were irradiated at CERN to a lower energy of 1.4 GeV proton beam but up to an equivalent radiation dose of 5×10^{15} protons. Because we missed an opportunity to deliver the grin lens to the CERN irradiation facility, the grin objective lens was instead irradiated at BNL by using a Co-60 source up to a total dose of $\sim 3 \times 10^6$ rad.

The reflectance of the Au-coated reflector and the transmittance of all other optics are measured at the wavelength of 830 nm before and after irradiation. Tables II shows the effects of irradiation up to an equivalent radiation dose of 10^6 rad on the reflectance and transmittance of the components of the optical diagnostic system. No noticeable change in the reflectance was observed on the Au-coated reflector even though the substrate of the reflector has turned nearly

opaque. The sapphire, 5 m long of illumination fiber, and 0.3 m long of imaging fiber, does not show any additional insertion loss. They are all radiation hard up to a 10^6 rad dose. However, the small grin objective lens did suffer radiation damage resulting in a 0.73 transmission. This tiny grin objective lens is made of silver-ion exchanged index modification internal to a glass substrate. Therefore, it was not anticipated to have a high radiation resistance. However, the advantage of its complex function in an extremely small size package outweighs the low radiation hardness disadvantage. Furthermore, it is well known that although glass (and silica fibers) loses its transmission in the visible wavelengths, near infrared (NIR) light can still has adequate light throughput for some applications.[8] This is also one of the reason we select NIR rather than visible laser light for backillumination of the mercury jet. Since the backilluminated NIR light passes this tiny grin objective only once, the 0.27 transmission loss over the entire experiment is tolerable and can be recovered with the present designed laser capability. We should note that the integrity of the imaging properties of the grin lens was unchanged, i.e., no image distortion was observed after the 10^6 rad radiation resistance test.

E. Scintillating fiber channel

A jacketed 2 m long 1 mm diameter blue emitting scintillating fiber is attached along with the imaging head to register gamma emission during the proton beam and mercury jet interaction. A 12 m long 1 mm diameter fiber patch cord (ThorLabs BFH37-1000) carries the blue scintillated light signal and is fiber coupled to an avalanche photodiode (ThorLabs APD210), designated as channel 0. The overall transmission at the center wavelength of 480 nm of the fiber patch cord is measured to be 0.77. The scintillating signal trace is displayed on an oscilloscope and data can be remotely retrieved from the control room. This scintillating signal serves to confirm the arrival of the proton beam and has the potential to extract the proton intensity from the scintillating signal pulse level.

In addition, charged particle detectors will monitor the flux of secondary pions produced to provide a measure of possible beam-induced reduction of density of the liquid jet.

F. Schematic of electronic trigger and high speed camera control

Because we are using several high speed cameras from different vendors, we must use separate camera control software for each camera. The limitation on their exposure time also requires two different sets of illumination laser pulse trains. A master trigger pulse, synchronized to the arrival of the proton bunch, is delivered to trigger the mercury loop system, the solenoid magnet system, and the optical diagnostic system together. The mercury jet reaches its steady state for 1 s when the solenoid magnet reaches the highest magnetic induction field of 15 T. However, there is a significantly long time lag of ~ 10 s for the solenoid system to power up to its full capacity. Therefore, the master trigger signal is first sent to a digital delay generator (Stanford Research DG535) to provide a sufficient long delay to synchro-
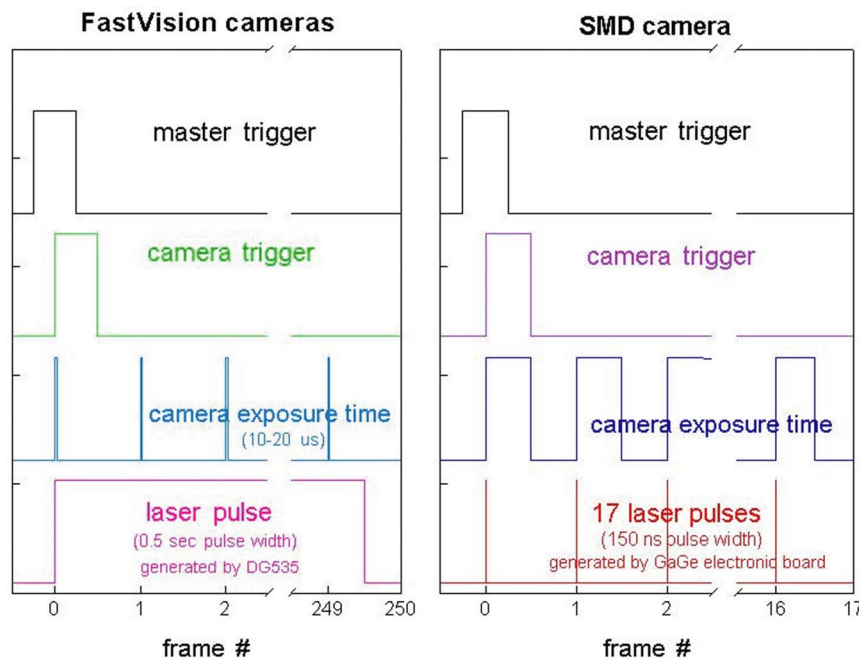
FIG. 4. (Color online) Schematics of synchronized signal of high speed camera and laser pulse.

nize with all other electronic components. These relative and absolute delays are measured by an oscilloscope. By adjusting each independent delay channel, complete synchronization of all cameras with the pulsing of the laser light sources can be achieved and verified by comparing the bright/dark image intensities of each frame of each CCD.

Figure 4 shows the two sets of pulse sequences used to simultaneously trigger all cameras. The 25 W infrared laser consisted of a 17 pulse sequences with a pulse width of 150 ns. This determines the exposure time of the SMD camera on the viewport 2. The laser pulse period is set to match the frame rate of the images. The SMD camera collects 16 frames of image.

Three 1 W lasers pulsed to a 0.5 s duration are used to independently illuminate viewport 1, viewport 3, and viewport 4, respectively. Typically, the FastVision and Olympus cameras continuously collect 260 frames of images. The exposure times on the cameras are set at $10-50$ μs, respectively, to give a sharp image quality. Although the sharpness of images increases with reduced exposure time, much more light is required for illumination. Therefore, a trade off between exposure time and laser intensity is made. On the contrary, the exposure time for SMD camera is determined by the laser pulse width. As the pulse width of the laser decreases, the laser intensity also decreases. In order to utilize the maximum allowable intensity of the 25 W laser, the maximum pulse width of 0.15 μs is used. This pulse width should not seriously jeopardize the image quality even running at its highest frame rate of 1 μs/frame. A schematic diagram linking all cameras, triggering electronics, and controlling computers is shown in Fig. 5. Two desktops reside in the control room to master the optical diagnostics system. All other electronics and desktops are placed in the TT2 tunnel adjacent to the interaction beam tunnel TT2A.

IV. INTEGRATED EXPERIMENTAL SETUP FOR HIGH POWER TARGET

A. Mercury loop system in solenoid magnet

The cross section and actual equipment for the mercury system with high field solenoid magnet is shown in Fig. 6. The horizontal line in Fig. 6(a) represents the proton beam. The Hg jet, which is ejected from right to left in Fig. 6(a), copropagates with the proton beam. Four viewports are shown within the solenoid bore, which represent viewing locations for observation of the Hg jet within its primary containment vessel (see Fig. 7). Viewport 2 is positioned at the center of the solenoid and is the location where the center of the proton beam interacts with the Hg jet. The Hg system provides for double containment vessel of the hazardous liquid metal and can be inserted or removed from the solenoid bore without disassembly. A hydraulic syringe pump, with a piston velocity of 3 cm/s, was used to pulse the mercury jet. This pump minimizes the heat added to the Hg as opposed to a centrifugal pump. The syringe pump also reduces the discharge pressure which is the limitation of a centrifugal pump. The Hg system provides a jet duration of a $\sim$3 s of constant velocity profile. A total of 180 kg of Hg is loaded in the system. A 30 KW, 200 bar hydraulic power unit drives the syringe pump.

The pulsed solenoid incorporates a magnetic induction field ramp up of 10 s and is capable of sustaining its peak field for a duration of approximately 1 s. A 5.5 MW, 700 V power supply delivers 7200 A of current to pulse the solenoid. The magnet is cryogenically cooled to 77 K prior to operation and warms up by 30 K during pulsing due to 30 MJ coil heating. Therefore, a 30 min cooling time is needed for each single shot. The magnetic axis is positioned at an angle of $\sim$67 milliradian to the proton beam, with the tilt provided by a common baseplate supporting all the equipment [see Fig. 6(a)]. The applied magnetic induction
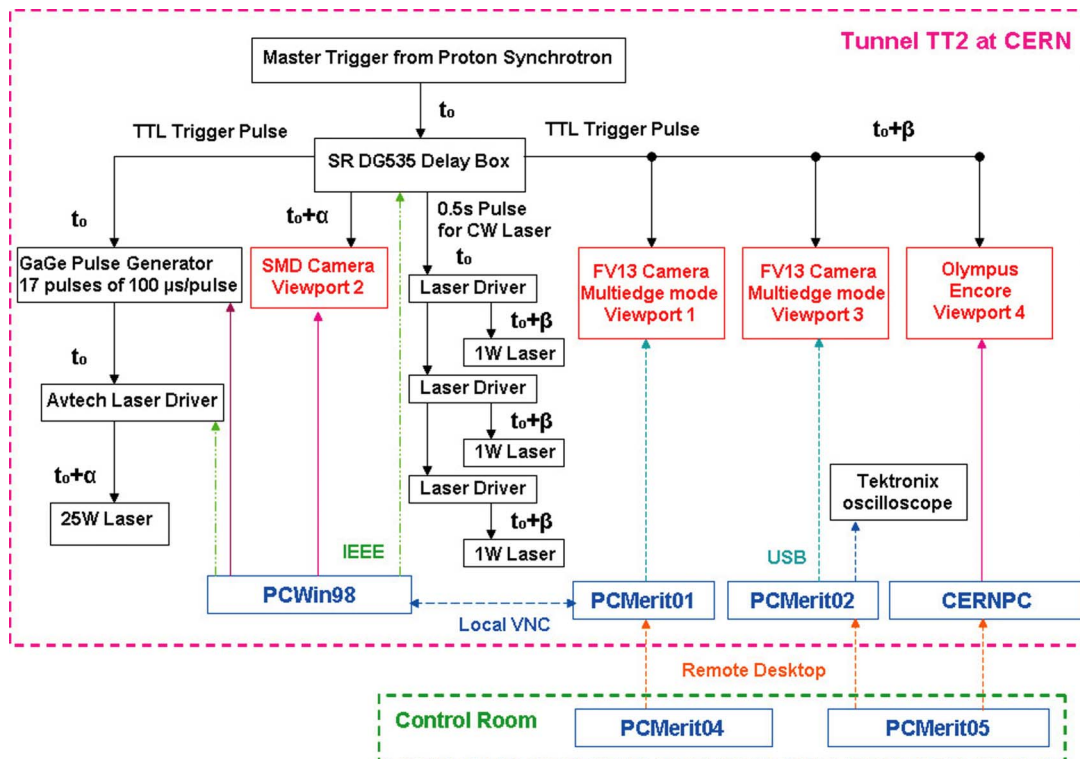
FIG. 5. (Color online) Schematics of electrical triggering and high speed camera control in the tunnel for the experiment.

field has been measured with gaussmeters placed both perpendicular and parallel to the magnetic induction field. The relationship between the measured magnetic induction field and the applied solenoid current was mapped to deduce the maximum magnetic induction field at the center of the solenoid. It was found that the maximum magnetic induction field reached 15 T.
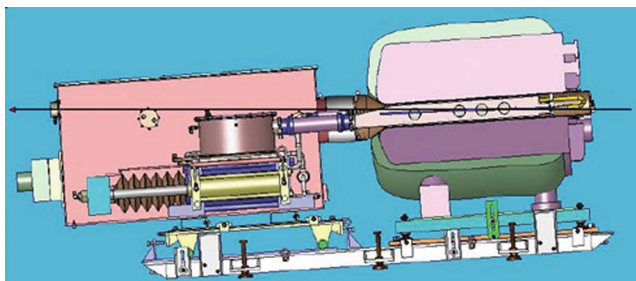
FIG. 6. (Color online) Photographs of the entire MERIT experiment. (a) Sectional side view of mercury loop system integrated with 15 T solenoid magnet. (b) Fabricated mercury loop system assembled with 15 T solenoid magnet (top view).

B. Water jet observation for nozzle performance test

Prior to mercury injection in the primary at Oak Ridge National Laboratory (ORNL), extensive optical diagnostics were carried out by pulsing water jets in the system by using four different types of nozzle configurations. One nozzle showed the most stable shape of jet motion with fairly uniform velocity, ~10 mm diameter and 20 m/s, respectively.

Due to the spray and wetting of water on the interior of windows, only ambiguous shadow of the water jet was observed. A clear surface motion is required in order to obtain accurate velocity measurement. Therefore, only qualitative diagnostics was made on the water jet. The field of view of each viewport is ~50 mm. The diameter of the jet is mea-
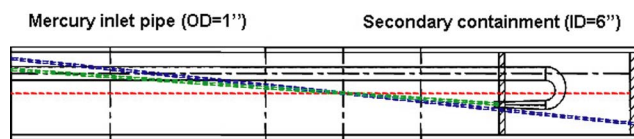

FIG. 7. (Color online) Geometry of viewports, showing the interaction between the mercury jet and the proton beam. (a) Top view. (b) Side view.
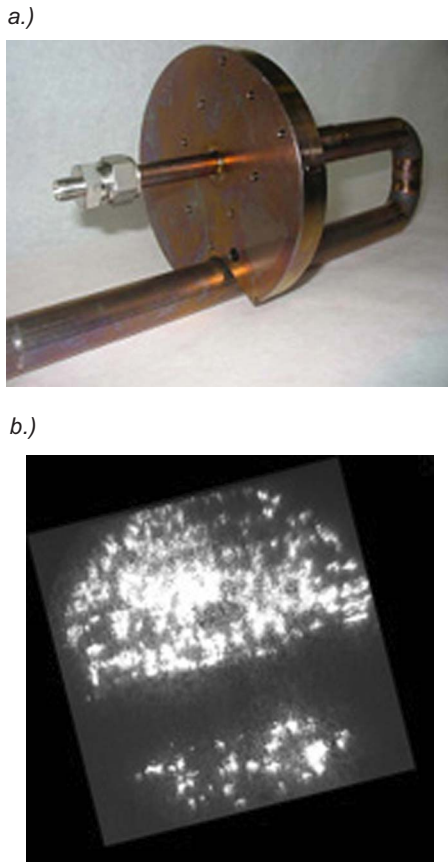
a.)

b.)

FIG. 8. (Color online) Photograph of Ti nozzle and observation of jet from nozzle at viewport 2. (a) Fabricated titanium nozzle. (b) Jet from titanium nozzle at viewport 2.
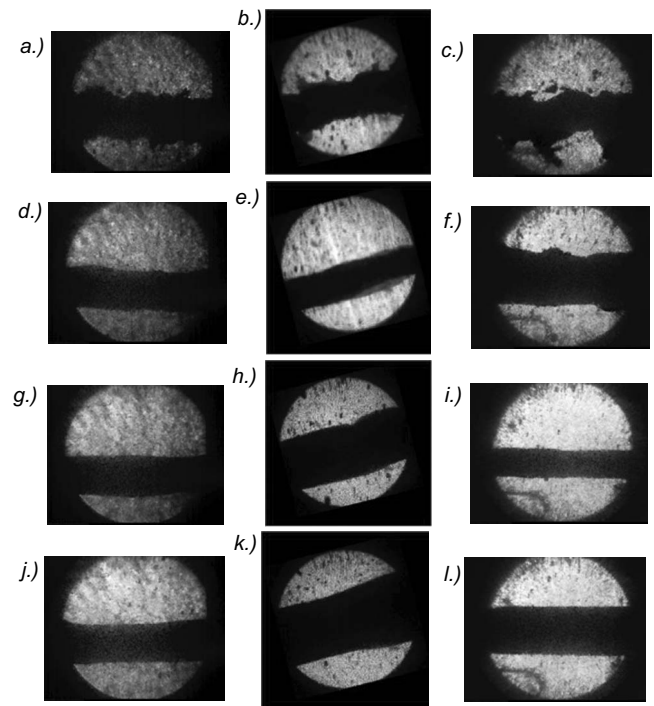

FIG. 9. Mercury jet flows as observed from the three viewports. The jet flows from right to left on each image. The first, second, and third columns represent viewports 1, 2, and 3, respectively. The individual caption shows the applied magnetic induction field. The jet velocity is 15 m/s. Images on viewport 2 has a 14° counterclockwise rotation due to the intrinsic SMD software issue. (a) $B=0$ T. (b) $B=0$ T. (c) $B=0$ T. (d) $B=5$ T. (e) $B=5$ T. (f) $B=5$ T. (g) $B=10$ T. (h) $B=10$ T. (i) $B=10$ T. (j) $B=15$ T. (k) $B=15$ T. (l) $B=15$ T.

sured by overlaying a grid of referenced field of view onto the images. The time lapse of each frame is read from the camera frame rates. The trajectory of the jet between several frames can then be directly measured and the velocity of the jet surface motion is estimated.

These measurements of the water jet tests were successfully done at ORNL. The observations led us to select the design of the final nozzle for the subsequent jet runs. Figure 8 shows the fabricated nozzle and the observation of the jet at viewport 2. It was fabricated from titanium and the assembly was anodized for electrical insulation.

V. OPTICAL DIAGNOSTICS RESULT

A. Image acquisition

Three tests of Hg jet run without a magnet and 14 complete integrated tests (i.e., with magnet, Hg loop system, and optical diagnostic system) were conducted at MIT with various values of the magnetic induction field (0, 5, 10, and 15 T) and two Hg jet velocities (15 and 20 m/s). Figures 9 and 10 are representative optical diagnostic results collected by the three cameras, with and without a magnetic induction field. Note that the Olympus Encore PCI 8000S camera for viewport 4 was not integrated in the MHD study done at MIT. It was replaced by a conventional video camera. Note that the results from the low speed camera such as conventional video camera are not included in this paper.

The current in the magnet system generates heat, which is cryogenically removed by using liquid nitrogen. As the magnet cools down, the all viewports become foggy due to condensation. It was found that ~ 0.5 l of water (from ORNL nozzle performance test) was not removed from the system prior to loading Hg. Flexible heater strips were installed both on the exterior of the primary containment vessel and on the snout in order to prevent the condensation of the humid air on the viewports. Although residual Hg droplets in sizes less than 1 mm often adhere to the sapphire viewports after every shot, jet motion with adequate image quality could still be collected.

B. Image processing

To measure the shape of the jet, 8 and 12 bit gray scaled TIF images are converted into digital forms. Background images are subtracted to reject the noise in the image digitization process. The residual data are then transformed into a 2 bit scaled image. Only the black and white colored pixels in the 2 bit depth images are used to differentiate the shadow of the jet and the background. A threshold is adjusted according to Otsu's method to highlight the interface between the mercury and the background.[9] Otsu's method, which relies on the assumption that all image pixels belong to one of two classes, background or foreground, has been shown to be efficient in image segmentation for bilevel thresholding.

The Hg jet was observed at upstream (viewport 1), midstream (viewport 2), and downstream (viewport 3) locations
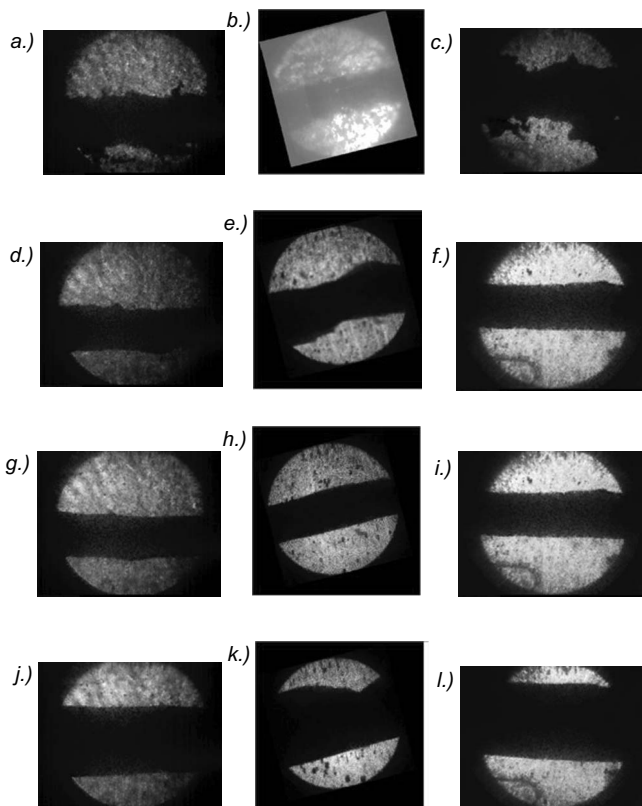
FIG. 10. Same as Fig. 9 but with a jet velocity of 20 m/s. (a) $B=0$ T. (b) $B=0$ T. (c) $B=0$ T. (d) $B=5$ T. (e) $B=5$ T. (f) $B=5$ T. (g) $B=10$ T. (h) $B=10$ T. (i) $B=10$ T. (j) $B=15$ T. (k) $B=15$ T. (l) $B=15$ T.
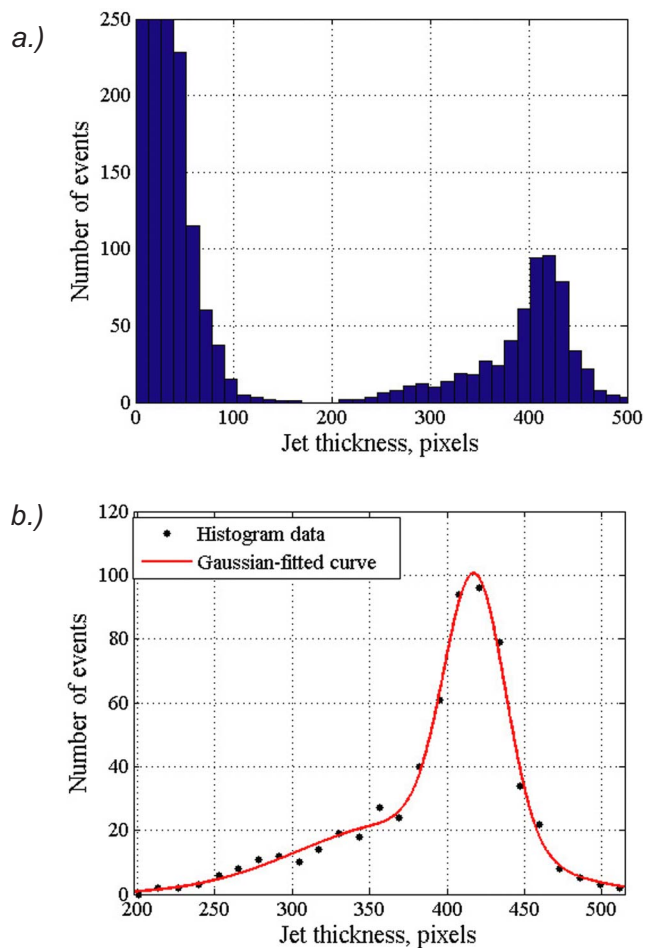

FIG. 11. (Color online) Jet thickness calculation from image analysis. (a) Histogram of number of events for the jet thickness measurement. (b) Fitted graph of histogram.

from the nozzle exit. (The locations of the viewports are shown in Fig. 7.) 220 images are collected at each run for both the upstream and downstream locations, with an image size of 1280×1000 pixels. The most probable transverse jet thickness within the longitudinal pixel range of 300–1000 is shown in the histogram of Fig. 11(a). Note that within this range, the transverse jet thickness probability P is obtained by counting the number of longitudinal pixel events in the jet image. If z denotes the transverse direction (in terms of pixels), the histogram in Fig. 11(a) can be written as follows [Eq. (1)] by using the least square curve-fairing approach:

$$P(z) = P_1 \frac{1}{\sqrt{2\pi}\sigma_1} e^{-(z-\mu_1)^2/2\sigma_1^2} + P_2 \frac{1}{\sqrt{2\pi}\sigma_2} e^{-(z-\mu_2)^2/2\sigma_2^2},$$

(1)

where μ_1, μ_2 the means, σ_1, σ_2 the standard deviations, and P_1, P_2 are the a-priori count of the histogram distribution. Note that, in pixel units, $\mu_1=418$, $\mu_2=371$, $\sigma_1=19.6$, and $\sigma_2=67.4$. The number of background events (i.e., outside of the jet) is always larger than that within the jet because the portion of bright background on each image is larger than that of the black jet shadow. The distribution on the left in Fig. 11(a) (i.e., $0 < z < 200$) represents the background pixels and is not included in the faired curve in Fig. 11(b).

On viewport 2, 16 image files are collected at each run, with an image size of 316×316 pixels. The images are analyzed in the same manner as described above. Viewports 1 and 3 give the same resolution for the images: 1280×1000. Thus, no image rescaling is needed when comparing the

pixel size for these images. However, viewport 2 gives a resolution of 316×316. Based on the 1 cm scale fiducial mark on the exterior of all viewports, all images taken on this viewport are rescaled to match the resolution of viewport 1 prior to comparison.

C. Motion and stability of the mercury jet in a magnetic induction field

Table III summarizes some of the results, showing the measured jet thickness at each viewport for various values of the magnetic induction field. When the jet is injected without an applied magnetic induction field, it is difficult to discern the jet surface because of blockage by Hg droplets on the

TABLE III. Measurements of jet thickness from nozzle (mm).

B-field (T)	Jet velocity (m/s)	Viewport 1	Viewport 2	Viewport 3
5	15	14.9	15.9	18.4
10	15	17.1	22.5	16.0
15	15	15.0	24.2	16.9
5	20	16.2	20.5	20.4
10	20	15.0	17.3	16.7
15	20	17.2	26.8	22.7

window. Therefore, some errors in the measurement exists [see the images in Figs. 9(a)–9(c) and Figs. 10(a)–10(c)]. On the contrary, when a magnetic induction field is applied, the measurement errors are significantly reduced, leading to significantly less intermittent jet boundaries. To obtain the jet velocity, the distance traveled by a fixed point on the jet surface is tracked over a given time period. Note that this velocity does not change with the imposition of a magnetic induction field. This explains why the pressure is approximately constant in the tube, consistent with Ref. 10. Note also that the accuracy of the velocity measurement deteriorates as the magnetic induction field increases. The inertial forces appear to dominate the jet movement when the jet velocity is 20 m/s. The turbulent jet motion is unstable but becomes stabilized as the magnetic induction field approaches 10 T. It has been reported that the radial force induced by the longitudinal component of magnetic induction field can significantly increase the jet thickness.[11]

At a jet velocity of 15 m/s, the relatively low inertial force reduces the extent of turbulent fluctuation. For this case, the magnetic induction field does not significantly affect the dynamics of the jet until the magnetic induction field strength of ~5 T is reached. Consequently, the thickness of the jet increases only slightly at 5 T. The results shown in Figs. 9 and 10 clearly suggest that the magnetic induction field has constrained (stabilized) the Hg jet flow by smoothing out the edges of the otherwise turbulent flow. At large value of the magnetic induction field (>10 T), stability is maintained at all viewports. At 15 T, a larger diameter (cross sectional distortion) is observed on all viewports.

The fact that the Hg jet size is relatively unchanged from 0 to 5 T but increases from 10 to 15 T suggests that the Hg jet encounters a different type of instability at higher field, namely, a quadrupole effect. The quadrupole effect would alter the jet's circular cross section to become elliptical. From the data obtained with a 20 m/s jet, the jet thickness at a 10 T is smaller than that at 15 T, which is manifested in the vertical elongation of the jet. The reduction of jet size on the minor axis of the elliptical core has to be accompanied by a gain in jet size on the major axis, in order to satisfy the continuity condition in flow. In other words, the cross-sectional area in flow should be constant. Although the two dimensional nature of the image data does not distinguish between an elliptical cross section and a circular one, occasional observation of a smaller jet thickness at 20 m/s with 10 T field as opposed to a 5 T indicates that the jet cross section might vary between the major and minor axes of an elliptical core. It is important to note that within the axial distance of interest, the jet diameter is approximately constant. Therefore, references to "larger jet diameters" should be interpreted to mean larger distortions of the jet cross section. As expected, jet motion in a magnetic induction field differently behaves, depending on the angle between the axis of the magnet and that of the jet, as a result of the differences in the magnitude of the components of the magnetic induction field.[12] Figures 12(c) and 12(d) show the transverse and longitudinal components of the magnetic induction field along the jet axis at different crossing angles. As the crossing angle increases, the transverse component of the magnetic induction field increases, but with no significant change in the longitudinal component. The increase in the transverse component of the magnetic induction field raises the induced current on the Hg jet. Therefore, the angle of the Hg jet is launched at 33 milliradian with respect to the axis of the magnet. A finite transverse component of the magnetic induction field still exists for the small crossing angle.[11] Note that the induced axial current leads to the generation of an azimuthal component of the magnetic induction field. At a jet velocity of 20 m/s, the jet thickness does not significantly change until 10 T. At a jet velocity of 15 m/s, the jet thickness does not significantly change until 5 T. These observations indicate that the ratio of the inertial to the magnetic force plays a key role in determining the jet thickness. This ratio is called Stuart number N, effectively showing the relative influence of the jet velocity and the strength of the magnetic induction field in a dimensionless form. Note that $N = \mathrm{Re}_m \mathrm{Al}$, where $\mathrm{Re}_m = \mu \sigma V L$, $\mathrm{Al} = B^2/\mu \rho V^2$. Re_m and Al are, respectively, the magnetic Reynolds number and the Alfvèn number. B, V, L, η, μ, σ, and ρ denote, respectively, magnetic induction field, mean velocity, diameter of jet, absolute viscosity, magnetic permeability, electrical conductivity, and density.

The observation from our work is supported by previous results. For example, several investigations have suggested that magnetic induction field suppresses turbulent fluctuations in conducting liquid by stabilizing the flow,[13–16] where stabilization is judged by an increase in the characteristic wavelength of the flow.

VI. CONCLUSION

In this paper, an optical diagnostic system based on backilluminated laser shadow photography is employed to investigate the mercury jet flow at velocities up to 20 m/s in magnetic induction fields up to 15 T. Synchronized short laser light pulses are used to illuminate the target and freeze the motion of the jet. A total of four optical imaging heads for each viewport are mounted on the exterior of the primary containment vessel. Three high speed cameras are used to simultaneously collect images on three viewports. An integrated all-in-one compact optical head, ball lens, illumination fiber, objective lens, and imaging fiber bundle are placed at the radius of curvature of a retroreflector, allowing for the illumination and image collection on one side of the mercury primary containment vessel. Due to the short time of frame rate, the time delay from light source to the arrival of camera CCD is adjusted considering the potential delay from the electronics as well as fiber optics. The calibration in timing accuracy is judged by the uniformity of consecutive collected image brightness based on the time difference of the triggered signal on the oscilloscope for the synchronization between cameras and laser. The calibration in timing accuracy of the proton beam to camera activation will be adjusted by the delay box based on the time difference between the response of scintillating channel and the triggering signal to camera at CERN experiment. The motion of mercury jet is
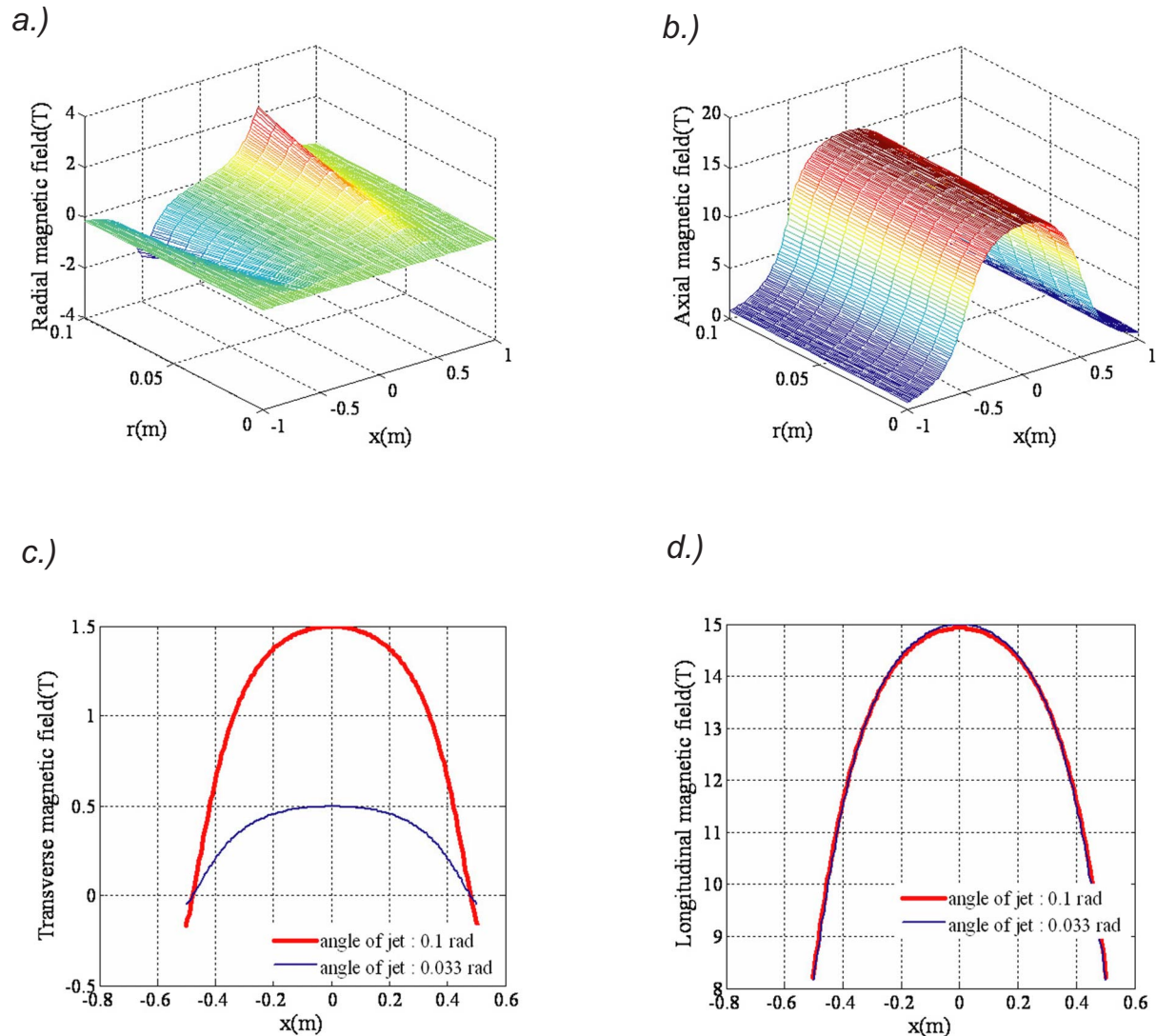
FIG. 12. (Color online) Calculated solenoid magnetic induction field map. (a) Radial field map. (b) Axial field map. (c) Transverse component of magnetic induction field along jet axis. (d) Longitudinal component of magnetic induction field along jet axis.

captured for durations of 0.5 s (viewports 1 and 3) and 1.6 ms (viewport 2), which enables us to give both the overall jet condition at upstream (downstream) and the accurate motion of jet at midstream, where the magnetic induction field is maximum and the center of beam-jet interaction is located. Image processing based on the probability approach leads us to give some information on the mercury jet thickness at various magnetic induction field strengths and velocities. As a result, the optical diagnostics as a key instrument in experiment provides how the ratio of the magnetic force to the inertial force effects to the cross-sectional distortion of mercury jet caused by the Lorentz force. In addition, the image analysis reveals the jet instability which might be caused by the strong induced axial magnetic induction field, which is possibly the onset of a quadrupole effect. Nevertheless, the experimental results clearly show that the magnetic induction field stabilizes the mercury jet by smoothing out the edges of the otherwise turbulent mercury flow. The comprehensive optical diagnostic method clearly allows us to have a better understanding of the behavior of a conducting jet moving in a high magnetic induction field environment. It

will play a key role as a primary diagnostic of free mercury jet interacting with 24 GeV proton beam under high magnetic induction field in high radiation area, i.e., the optical diagnostic will allow us to interpret the beam-jet interaction length caused by the energy deposition from the proton beam as well as the splash velocity on the mercury jet surface with the aid of the high speed camera.

Upon the successful completion of the pulsed mercury jet in the high magnetic induction field at the MIT Plasma Science and Fusion Center, the equipment was shipped and placed in a 24 GeV proton beam tunnel at CERN. The MERIT experiment has entered its final but the most interesting phase as a proof-of-principle experiment to address target issues facing the construction of neutrino factories and muon colliders.

[1] H. Kirk, K. Brown, R. Fernow, C. Finfrock, D. Gassner, G. Greene, S. Kahn, B. King, R. Prigl, R. Samulyak, J. Scaduto, N. Simos, P. Thieberger, T. Tsang, H. Wang, R. Weggel, A. Bernandon, A. Fabich, J. Lettry, H. Ravn, A. Zeller, D. Beshears, M. Cates, J. Haines, B. Riemer, P. Spampinato, J. Tasi, K. McDonald, and Y. Fukui, *Proceedings of the 2001 Particle Accelerator Conference*, Chicago. IL, June 18, 2001, p. 1535.

[2] V. Graves, P. Spampinato, T. Gabriel, H. Kirk, N. Simos, T. Tsang, K. McDonald, P. Titus, A. Fabich, H. Haseroth, and J. Lettry, *Nuclear Instruments and Methods in Physics Research Section A: Accelerators, Spectrometers, Detectors and Associated Equipment*, 2006, Vol. 562, p. 928.

[3] N. V. Mokhov, Fermilab Technical Report No. FERMILAB-Conf-00/208 (2000).

[4] A. G. Fedin, Magnetohydrodynamics (N.Y.) **9**, 301 (1973).

[5] A. J. Mackinnon, C Niemann, K. Piston, G. Holtmeier, T. McCarville, G. Jones, I. Reinbachs, R. Costa, J. Celeste, R. Griffith, R. K. Kirkwood, B. J. MacGowan, and S. H. Glenzer, Rev. Sci. Instrum. **77**, 10E529 (2006).

[6] L. A. Dorf, A. L. Roquemore, G. A. Wurden, C. M. Ticos, and Z. Wang, Rev. Sci. Instrum. **77**, 10E517 (2006).

[7] N. Simos, BNL review, BNL (2005), URL http://www.hep.princeton.edu/~mcdonald/mumu/target/simos/Simos_121205.pdf.

[8] T. Kakuta, T. Shikama, and M. Marui, *Seventh International Conference on Nuclear Engineering*, Tokyo, Japan, 1999, p. 19.

[9] N. Otsu, IEEE Trans. Syst. Man Cybern. **9**, 62 (1979).

[10] V. Graves, MUTAC review, ORNL (2007), URL http://www.hep.princeton.edu/~mcdonald/mumu/target/graves/VGraves-070418.pdf.

[11] J. Gallardo, S. Kahn, R. B. Palmer, P. Thieberger, R. Weggel, and K. McDonald, Muon BNL Technical Note MUC-NOTE-TARGET-242 (2002).

[12] R. Samulyak, MUTAC review, BNL (2006), URL http://www.hep.princeton.edu/~mcdonald/mumu/target/samulyak/mutac06_samulyak_targetsimulations.pdf.

[13] V. A. Bernshtam, S. V. Kozyrev, and A. I. Él'kin, Magnetohydrodynamics (N.Y.) **18**, 132 (1982).

[14] S. V. Kozyrev and A. I. Él'kin, Magnetohydrodynamics (N.Y.) **17**, 353 (1981).

[15] J. A. Shercliff, J. Fluid Mech. **13**, 644 (1956).

[16] R. R. Gold, J. Fluid Mech. **13**, 505 (1962).